Full paper

High-efficiency self-charging smart bracelet for portable electronics

Yu Song[a], Haobin Wang[a], Xiaoliang Cheng[a], Guoke Li[c], Xuexian Chen[a,b], Haotian Chen[a], Liming Miao[a], Xiaosheng Zhang[c], Haixia Zhang[a,b,*]

[a] National Key Lab of Nano/Micro Fabrication Technology, Institute of Microelectronics, Peking University, Beijing 100871, China
[b] Academy for Advanced Interdisciplinary Studies, Peking University, Beijing 100871, China
[c] School of Electronic Science and Engineering, University of Electronic Science and Technology of China, Chengdu 611731, China

ARTICLE INFO

ABSTRACT

The rapid advancements of lightweight, customized electronics have imposed a significant challenge on sustainable and maintenance-free micro-energy systems. For the sake of solving the limited power supply and low integration, it seems urgent to develop the flexible energy devices through structure design and performance optimization. Here, a high-efficiency self-charging smart bracelet is proposed by seamlessly combining flexible freestanding triboelectric nanogenerator, power management module with stretchable double-sided micro-supercapacitors. For energy-generating component, the FPCB-based freestanding triboelectric nanogenerator and power management module are adopted with excellent output performance, which obtains peak voltage of 305 V, and maximum power efficiency of 69.3%. Additionally, the double-sided micro-supercapacitors based on CNT-PDMS elastomer are designed to work stably and reliably as the stretchable energy-storing component, the capacitance of which maintains more than 96.87% even under 20% stretching strain. During human normal motions, this smart bracelet could be utilized for scavenging random motion movements and then simultaneously storing in the energy storage device through the high-efficiency power management module to develop a self-powered system for portable devices. As an effective and efficient power supply solution, this proposed self-charging smart bracelet demonstrates admirable potential to power a temperature-humidity meter or pedometer, which owns huge potentials in micro-energy wearable electronics and lays the solid foundation on the smart appliance.

1. Introduction

As the explosive development of multifunctional devices and wearable technologies [1–4], mandatory demands of portable, lightweight and attachable power units have attracted huge attention. For wearable practical demands, combining the harvesting and utilization of mechanical energy from human motion with high-efficiency in situ wearable energy storage is crucial and promising for its sustainability and inexhaustibility [5–8]. However, confronted with complicated external circuit and separated component, traditional energy system lacks in flexibility, comfort and free-maintenance, which brings difficulties in smart devices and miniaturized applications. An innovative strategy is to assemble energy-generating devices [9,10] and energy-storing devices [11,12] with power management design and compose the self-charging power unit for continually driving portable electronics [13–18]. As for different types of energy-generating modes [19–21], triboelectric nanogenerators (TENGs) as the creative invention perform an ideal method to convert mechanical energy from irregular body movements into electricity based on the coupling effect of electrostatic induction and triboelectrification [22–25]. Compared to other working mechanism, freestanding configuration is facile to be optimized, which could overcome the material limitation and working space constraint with stable output performance [26,27].

With regard to energy-storing devices, supercapacitor is considered to have wide potential prospects, which possesses cycling stability, fast charging rates and biocompatibility [28,29]. Unfortunately, conventional supercapacitor with sandwiched structure limits its application in large-scale fabrication and system integrity, which requires the energy storing components with similar dimensions. Recently, the micro-supercapacitor (MSC) [30–33], has drawn huge attentions in on-chip electronics and microsystem. With in-planar layout and the elimination of the separator, the MSC could allow more active materials loaded and decrease the diffusion length greatly. Through the structure optimization (double-sided layout) and material selection (porous conductive elastomer), the electrochemical performance and the integration with micro energy device could be significantly improved at the same time

[34–36]. Afterwards, assembled with freestanding TENG and double-sided MSCs, self-charging power unit could drive portable electronics. However, working as a capacitive-behavior energy harvester, TENG owns a high inherent impedance with high voltage and low output current. These characteristics result in low energy transfer efficiency for either powering electronics directly or charging energy storage device (battery/capacitor) due to the relatively low impedance. Consequently, an universally matched power management design is required for connecting energy-generating component with energy-storing component to power portable electronics sustainably [37,38].

Herein, we demonstrate a high efficiency self-charging smart bracelet (SCSB) involving the energy-generating component, power management module and energy-storing component for portable electronics. Taking advantage of elastomer transferring and in-planar layout, we optimize the double-sided micro-supercapacitors (D-MSCs) based on carbon nanotube-polydimethylsiloxane (CNT-PDMS) conductive elastomer, which demonstrates stable electrochemical performance and mechanical robustness. Meanwhile, by utilizing FPCB technique, the freestanding triboelectric nanogenerator (F-TENG) and corresponding power management module (PMM) are proposed and fabricated together, which could harvest human motion energy effectively and efficiently. By seamlessly assembling the D-MSCs with F-TENG and PMM, the conformal SCSB is prepared, which owns stretchability, flexibly and compatibility. Additionally, we successfully demonstrate this SCSB for scavenging walking energy and sustainably driving a pedometer and humidity-temperature meter to obtain the smart energy system. Therefore, this prototype of self-charging portable device presents great potential in practical and sustainable energy system.

2. Results and discussion

2.1. Design of high-efficiency self-charging smart bracelet

The high-efficiency self-charging smart bracelet for powering the wearable/portable devices is schematically illustrated in Fig. 1. Our proposed SCSB could be directly worn among the wrist with portability and artistic design. The detailed structure of the SCSB is depicted in Fig. 1a, which seamlessly integrates the freestanding triboelectric nanogenerator, power management module, double-sided micro-supercapacitors and portable electronics in series among the Ecoflex substrate. As shown in Fig. 1b, this flexible SCSB could easily convert the mechanical energy from arbitrary human movements into the electrical energy via energy-generating component (F-TENG). Meanwhile, the generated electrical energy could be efficiently transferred and directly stored into energy-storing component (D-MSCs) through the power management module, which could sustainably drive wearable/portable electronics. The performance of each component of the SCSB is evaluated individually before the ultimate operations. Specifically, for the energy-storing component, the D-MSCs are conducted based on the porous CNT-PDMS conductive elastomer, which is prepared through solution-evaporation method (Fig. S1, Supporting information). SEM images in Figs. 1c–1d clearly demonstrate the morphologies of the sugar templates and their corresponding porous structure, which possesses an open network with large surface area. Meanwhile, with the proper sugar ratio [33], the porous network could be successfully formed after sugar dissolution. After the gel electrolyte coating, the SEM image in Fig. 1e proves that the electrolyte is penetrated into the porous structure and CNTs are exposed, which could efficiently form the conductive network and guarantee the electrochemical performance.

2.2. Performance of the stretchable D-MSCs for energy storage

As for the energy-storing component, it seems crucial to meet the demands of complicated operating environments. Here, a stretchable and flexible Ecoflex based D-MSCs is designed and prepared through laser patterning and elastomer transferring process with CNT-PDMS conductive elastomer. Configured with in-planar and double-sided structure, the thickness of the whole device could be decreased. Firstly, PMMA mold is laser patterned with interdigital design and CNT-PDMS-sugar mixture is poured into the grooves. Then Ecoflex elastomer is poured among the surface and peeled off with solidified CNT-PDMS-
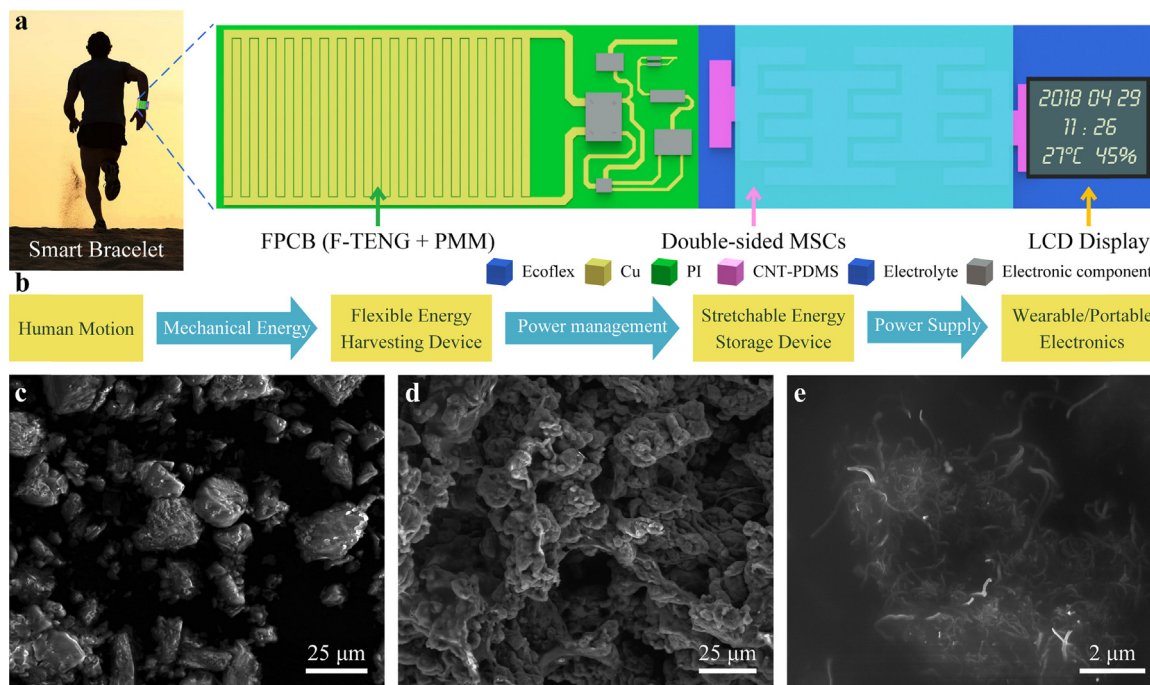
Fig. 1. a) Schematic diagram of high-efficiency self-charging smart bracelet configured with freestanding triboelectric nanogenerator, power management module, double-sided micro-supercapacitors and portable electronics. b) Working mechanism of smart bracelet with mechanical energy harvesting, power management and stable energy storing for portable electronics. SEM images of morphology of c) sugar templates, d) corresponding porous structure of CNT-PDMS elastomer and e) exposed CNTs coated with gel electrolyte.
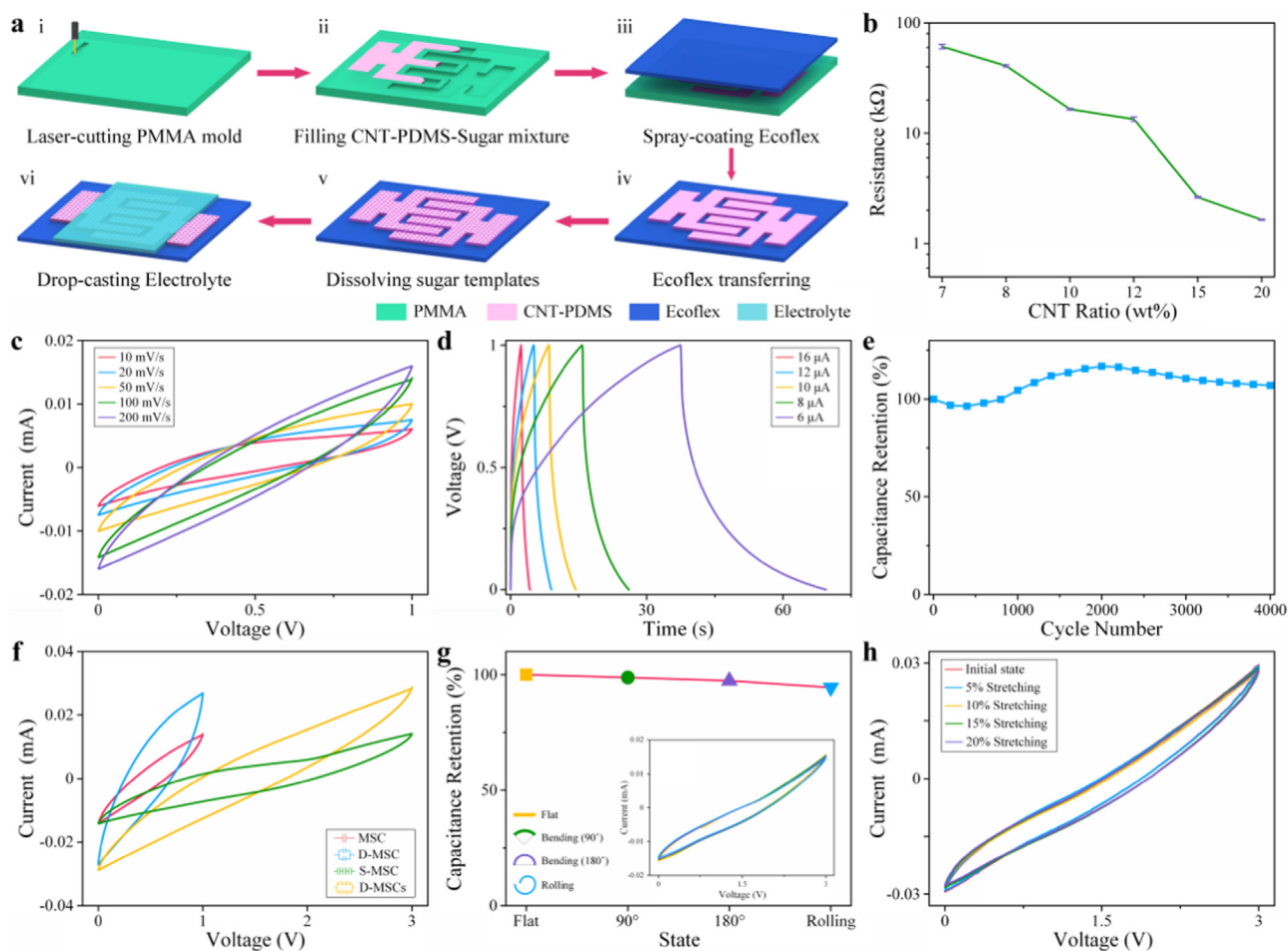
Fig. 2. Performance of the double-sided micro-supercapacitors for energy storage. a) Fabrication process of stretchable MSC based on CNT-PDMS elastomer. b) Initial resistance of CNT-PDMS conductive elastomer with different CNT contents. Electrochemical behavior of single MSC, c) CV curves at different scan rates, d) GCD curves with different charging currents, and e) cycling stability after 4000 cycles. f) Comparison of MSCs with different connection under the scan rate of 100 mV/s. Performance stability of D-MSCs under various types of deformations. g) Capacitance retention under different bending states (with inset image showing the corresponding CV curves), and h) CV curves under different stretching strains (up to 20%).

sugar mixture together. After the sugar dissolution, gel electrolyte is drop casted and MSC could be developed. The fabrication method for the D-MSCs is illustrated in Fig. 2a and further discussed in the Experimental Section.

The Fig. S2 in the Supporting information clearly shows that MSC owns a well-defined shape, which could be easily rolled up and stretched in portable electronics. Additionally, the cross-sectional SEM image of the device shows the bottom-up structure composed of elastomer substrate, active material layer and solid-state electrolyte film. For the CNT-PDMS conductive elastomer, Fig. 2b demonstrates the original resistance variation among different CNT contents. With the CNT content increases, the resistance decreases significantly with the smaller resistivity. Then we choose CNT-PDMS conductive elastomer with CNT content of 20% as the active material.

To evaluate the electrochemical behavior, the MSC is carefully carried out through cyclic voltammetry (CV), galvanostatic charge-discharge (GCD), and cycling stability measurements via electrochemical workstation at room temperature. For the individual MSC, CV curves with the scan rates from 10 mV/s to 200 mV/s are recorded at the specific potential window. As shown in Fig. 3c, CV curves are symmetrical about the zero-current line, which could be obtained attributed to the intrinsic characteristic of the carbon-based materials, proving the double-layer electrochemical behavior. Then the typical GCD curves are demonstrated in Fig. 3d, the charging/discharging currents of which are from 6 μA to 16 μA. Evidently, the discharging

time is same with their corresponding charging counterparts, as well as their linear voltage-time profiles. Due to the compromise between the strechability and electrochemical performance, we utilize the Ecoflex as the substrate instead of electrolyte, which exerts negative influence on the performance to some extent. As for the cycling stability, Fig. 3e indicates the capacitance variation of the MSC device with in-planar interdigital electrodes under the charging cycles (100 mV/s). It is worth noting that the capacitance of the device increases at the beginning due to the electrode self-activation process. Then it decreases gradually and retains about 107% after 4000 cycles compared with initial capacitance.

In general, to improve the integration and produce required potential range and capacitance for practical applications, MSCs are connected in serial on one side and in parallel on double sides of an Ecoflex substrate, respectively. Electrochemical performance comparison between MSC devices with four types of connection (MSC, S-MSC, D-MSC, D-MSCs) is evaluated, the schematics of which are shown in Fig. 2f. From this image, CV curves (100 mV/s) demonstrate that an enhanced potential range up to 3 V by serial connection could be provided, meanwhile, the output current of double-sided parallel connection approximately doubles the current of single-sided connection. Definitely, the potential range and its working current can be improved by connecting MSC units in serial or in parallel to meet the demands of the power and energy density. For galvanostatic charging/discharging current (16 μA), D-MSC doubles the charging/discharging time
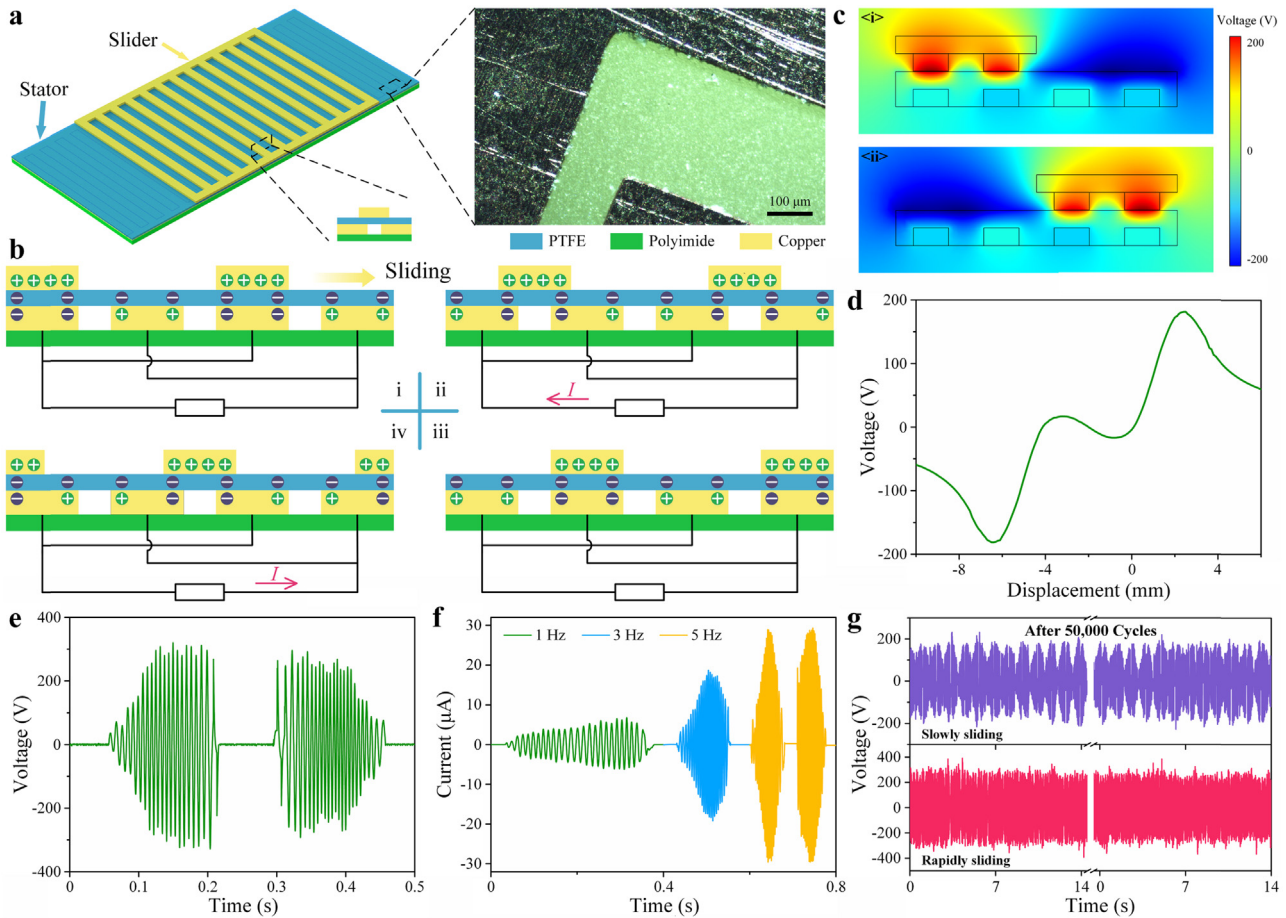
Fig. 3. Performance of freestanding triboelectric nanogenerator for harvesting mechanical energy. a) Diagram and definition of FPCB based F-TENG, and the microscope image of the comb electrodes. b) Working mechanism and charge distribution of the F-TENG in contact-sliding mode with four states. c) The simulated potential distributions during sliding process with d) the detailed results reflecting the working process. e) The typical electrical output voltage of the F-TENG during one-cycle sliding process. f) Waveforms of output currents of F-TENG under different working frequencies. g) Cycling reliability of output performance of F-TENG after 50,000 cycles under slowly and rapidly sliding.

compared with MSC; while for D-MSCs, it maintains the same charging/discharging time and the potential range is further increased by three folds compared with D-MSC (Fig. S3a, Supporting information).

Besides, as the areal capacitance is the precise evaluation for the electrochemical capability of MSC, it is calculated based on the following Eq. (1) from the CV curves of different MSCs:

$$C_A = \frac{Q}{A \cdot \Delta V} = \frac{1}{p \cdot \Delta V} \int_{V_1}^{V_2} I(V) dV, \tag{1}$$

where $I(V)$ is the charging/discharging current function, A is the area of the MSC, p is the scan rate, ΔV is the potential window during the discharge process, and V_1 and V_2 are maximum and minimum voltage values, respectively. Fig. S3b (Supporting information) compares the areal capacitance, where D-MSC could obtain maximum areal capacitance of 263.66 μF/cm² at the scan rate of 10 mV/s, which decreases slightly with the increase of the scan rate. Obviously, the capacitance of S-MSC is only one third of MSC device and that of D-MSC is two times over the MSC. Assisted by the porous structure with large surface area and highly conductive elastomer, the D-MSCs demonstrates great electrochemical behavior and enhanced working capability with reliable areal capacitance.

To evaluate the mechanical property of D-MSCs, several flexibility tests are performed under various types of deformations. Firstly, under different bending conditions, the capacitance demonstrates negligible changes compared to the initial state shown in Fig. 2g. The inset image shows negligible degradation of CV curves at 100 mV/s can be observed

when the D-MSCs are bent or rolled up at different angles, suggesting the reliable mechanical stability. The device is then bent at 90° for 1000 cycles, and CV test indicates that the areal capacitance remains 99.4% retention of the initial capacitance, as shown in Fig. S3c (Supporting information). In addition, when assembled into the smart bracelet, the D-MSC device requires to work reliably under stretched states. To demonstrate the stretchability of electrode, we evaluate the resistance stability with repeated stretching-releasing cycles. During 1000 stretching cycles, the electrode experiences little deviation even under 50% stretched state shown in Fig. S4 (Supporting information), the ideal strain-tolerant capability of which is crucial to the whole device. As shown in Fig. 2h, the D-MSCs shows no noticeable performance degradation in the CV curves (100 mV/s). The normalized capacitance, calculated from the corresponding CV curves, exhibits highly stable performance within a variation of 96.87% under 20% stretching strain compared with the initial state (Fig. S3d, Supporting information). Therefore, these tests confirm the excellent flexibility and stretchability of the D-MSCs, which is mainly attributed to the stretchable Ecoflex substrate, and the intimate and strong binding of the coating materials (CNT-PDMS elastomer) with the substrate, showing promising potential in self-charging smart bracelet for wearable systems.

2.3. Performance of the F-TENG for energy generating

The structure of freestanding triboelectric nanogenerator for energy-generating component is presented in Fig. 3a, where the device is

mainly composed of two parts: a freestanding triboelectric layer with grating segments as slider and two comb electrodes as the stator. To obtain a strong electrification during contact, PTFE and copper are selected as the materials for the freestanding triboelectric layer and metal electrodes, respectively, according to the triboelectric series. The fabrication of the F-TENG is developed through the FPCB technique, the detailed process of which is discussed in Fig. S4 (Supporting information). As for the metal-electrode part, the FPCB-based copper electrode is patterned into complimentary comb structures with the same periodicity. After the lamination of PTFE film, comb electrodes with electrification material are successfully obtained. The optical microscope image clearly illustrates that the electrodes own a well-defined shape and sharp boundaries, where the detailed parameter of F-TENG is presented in Fig. S5 (Supporting information).

The working mechanism of the F-TENG can be explained as the coupling of contact electrification and in-planar sliding induced charge transfer (Fig. 3b). Initially, the grating rows of the slider Copper layer are brought into contact with the stator layer at a fully overlapping position of odd-line electrode (Fig. 3b < i >). Considering the fact that copper is more triboelectrically positive than copper, contact electrification occurs between PTFE and copper layers, which brings in negative charges on the PTFE surface and positive charges on the copper. Obviously, there is no charge flowing between the stator electrodes due to the electrostatic equilibrium at this state. When the slider layer begins to slide rightward, this slider layer gradually moves from the overlapping position of stator layer (Fig. 3b < ii >). As a result, an electric potential drop is generated, which drives negative charges flow from the odd-line electrodes to the even-line electrodes along with the sliding motion, and induces a transient current in the external circuit at the same time. Once the slider layer moves to the fully overlapping position with stator layer of even-line electrode (Fig. 3b < iii >), all of the negative charges transfer to even-line electrode, with another electrostatic equilibrium achieved. When the slider layer continues to slide leftward (Fig. 3b < iv >), the positive charges will spontaneously flow back to odd-line electrodes, producing a reverse current in the external load. Therefore, the whole charge transferring cycle is completed, the working principle of which could be further confirmed by simulation (COMSOL Multiphysics) based on finite-element method (Fig. 3c). Consistent with the location of slider layer, the charge distribution profile changes as theoretically expected, which could generate corresponding alternating signal output according to the simulation shown in Fig. 3d.

As for the output characterization of F-TENG, open-circuit voltage, short-circuit current and mechanical robustness are evaluated through the oscilloscope. Notably, during the single unidirectional sliding process, the total effective area increases while the slider moves inwards, resulting in an increasing oscillation behavior of output signal. Then the maximum amplitude is generated when all triboelectric parts are involved in the process, which induces the triangular waveform as shown in Fig. 3e. In addition, with short PTEF layer, the total effective area decreases quickly once the Cu slides outwards. In order to make electricity generation more efficient and maintain the maximum effective area during the sliding process, we fabricate an extended stator layer compared with slider layer. In this design, the slider layer will always slide within the range of the stator electrodes with enhanced performance, where each unit step of sliding transfers almost the same amounts of charges without any decay during the sliding process. Obviously, such freestanding layout demonstrates advantages in collecting large-scale motion energy compared to the single-electrode TENG. The F-TENG reaches the peak voltage of 305 V, and the amplitude changes with the overlap ratio between the slider layer and the stator layer. The signal polarity in the envelope waveform oscillates rapidly along the sliding direction. Despite the fact that the input mechanical motion occurs once along a single direction, the number of charge transfer multiplies with the grating pattern structure. Apparently, this behavior of F-TENG is consistent with the theoretical simulation.

Additionally, the output short-circuit currents produce similarly triangular waveforms (Fig. 3e). When the frequency of the sliding process are 1 Hz and 5 Hz, the maximum instantaneous currents are 6.79 μA and 29.35 μA, respectively. For a single-direction sliding input, faster sliding velocity inevitably exerts larger instantaneous current values and shorter output operating times. Considering the fact that the flexible printing circuit board is thin and lightweight enough, such energy generating capability is satisfying. To further meet the demands of continuous energy harvesting during human motion, this flexible and uniform layout enhance the integrity and robustness for the F-TENG. For the cycling stability, when the devices are performed continuously for 50,000 cycles, the device experiences little decay in the output performance under the both slowly and rapidly sliding process (Fig. 3g). The SEM images of the PTFE morphologies during the sliding period demonstrates negligible damage occurred among the surface, which further proves its long-time stability (Fig. S7, Supporting information). Besides, under normal human motions, the corresponding output performance is evaluated with various operations (Fig. S8, Supporting information) to verify the reliability in practical applications.

2.4. Performance of power management module for F-TENG

In order to obtain the maximum output energy from the F-TENG, the power management module (PMM) should be optimized including two parts: the effective energy output of F-TENG and maximum transferred energy output for storage. The detailed analysis for the boosting method is discussed in Note S1 (Supporting information) [37]. For the first part, to obtain the cycles for maximized energy output of F-TENG, we adopt the serial-switch design, which is controlled by logic circuits [39,40] triggered by the peak value of rectified voltage. The precise control of the switch is crucial for the PMM which should be turned on once the rectified voltage reached its peak value as the comparator. The detailed circuit diagram and operation principle is shown in Fig. S9 (Supporting information). For the second part, we employ the LC oscillating system to transfer the stored energy efficiently, which could be analyzed using the zero-input response model (the detailed circuit diagram and corresponding simulation results illustrated in Fig. S10, Supporting information). According to the simulation, negligible energy loss is produced in a quarter of a cycle, during which time, the energy in C_{TENG} is transferred to the inductor successfully.

The detail working process of PMM can be separated into six states as shown in Fig. 4a based on the transferred charge Q, built-up voltage V and relative displacement X. In state i, the slider part begins to move to $X = X_{max}$ at switch-off, enabling enable $(Q,V) = (0, V_{OC, Max})$; in state ii, turn on the switch to transfer the stored energy from F-TENG to inductor via LC oscillating, enabling $(Q,V) = (Q_{SC, Max},0)$; in state iii, turn the switch off and the slider part moves towards $X = 0$ from $X = X_{max}$ towards, therefore, the stored energy is further transferred to the external capacitor from the inductor; in state iv, the slider part reaches to $X = 0$, enabling $(Q,V) = (Q_{SC, Max}, -V'_{Max})$; in state v, the stored energy in F-TENG is transferred to inductor via LC oscillating again at switch-on, enabling $(Q,V) = (0, 0)$; in state vi, turn the switch off and the slider part moves from $X = 0$ towards $X = X_{max}$ at switch off, transferring the stored energy to the capacitor at the same time. Within the six-state operations, we could accomplish the maximized energy generating and transfer efficiency for further energy storage.

To further demonstrate the feasibility of high-efficiency PMM for F-TENG, we develop the F-TENG assembled with PMM during the general FPCB technique and the performance is evaluated as follows. Compared with the normally standard circuit (full-wave rectifier), the charging capability of the PMM could be clarified clearly. Considering the easy selection of capacitors with various capacitance, we utilize series of commercial capacitors ranging from 2.2 μF to 4.7 mF to verify the general charging possibility. Firstly, the charged voltages of 10 cycles under the PMM and standard circuit are shown in Fig. 4b, respectively.
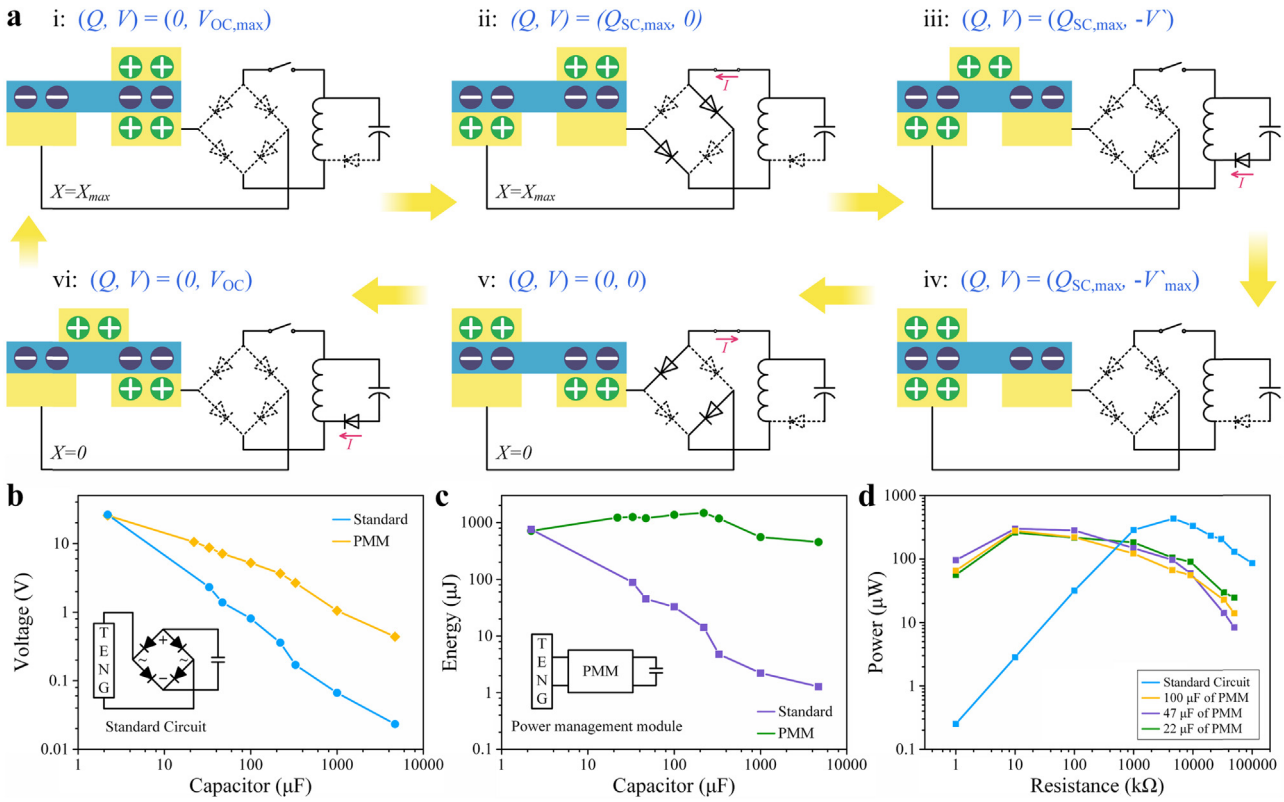
Fig. 4. Schematic illustration of power management module for F-TENG. a) Operating cycles for scavenging maximum energy from F-TENG and transferring it to capacitor via LC oscillating. Comparison of b) the charging voltages and c) stored energies for capacitor ranging from 2.2 μF to 4.7 mF of the F-TENG between a standard circuit and the PMM. d) The AC power curve of F-TENG and experimental DC power curve via PMM for different capacitors.

Obviously, both of them decrease gradually with the capacitance increasing, while the charging voltage of PMM is higher than that of standard circuit. For the capacitor with 4.7 mF, 0.44 V and 0.023 V could be obtained through the PMM and standard circuit, respectively, resulting in the fact that the charging voltage of PMM is 19.13 times of rectifier effect. Additionally, the stored energy ($E = 1/2CV^2$) by PMM maintains stable and degrades a little from 757.78 μJ to 454.96 μJ, however, the stored energy by standard circuit decreases significantly from 716.59 μJ to 1.28 μJ as the capacitance increases from 2.2 μF to 4.7 mF as plotted in Fig. 4c. Obviously, cooperated with a capacitor of 4.7 mF, the stored energy by PMM is 379 times higher than the rectifier circuit. In practice, we prefer to utilize a large capacitor or supercapacitor to store the energy harvested by F-TENG, therefore, PMM is capable of transferring higher energy to the large capacitor in specific application.

Meanwhile, for a practical working F-TENG, the maximum output power (P) under different external load, is crucial to evaluate TENG's performance. As the continuous power management module, the total power efficiency η_{total} plays the significant role for the characterization of PMM, which is defined as the ratio of the maximum DC power stored in the external unit to the maximum AC power delivered to a resistive load generated by the F-TENG [37,40]. To measure η_{total}, we firstly obtain the maximum AC power extracted by measuring the Root-Mean Square value of current using resistance with different values and then calculating the effective power by equation $P = I^2R$. As shown in Fig. 4d, the maximum AC power generated by F-TENG is 433.33 μW at a matched load resistance of 4.7 MΩ. Afterwards, for different capacitors, the DC power is calculated by the equation $P = V^2/R$, and a maximum DC power is performed at the equivalent resistance of 10 kΩ with the capacitance of 47 μF. Thus, the whole efficiency of PMM for F-TENG is calculated to be 69.3%. Correspondingly, the DC power reaches maximum of 260 μW and 279 μW at the approximate resistance of 10 kΩ

with the capacitance of 22 μF and 100 μF, respectively. Notable, this PMM shows good consistency for different capacitors and the optimal resistance of TENG is significantly decreased from 4.7 MΩ to 10 kΩ. Meanwhile, the DC power curve is relatively flat, which performs a wide range of resistance with great power output. Therefore, the PMM has broadened the optimal matching resistance and enhanced the energy transfer efficiency, making the great step towards the practical electronic devices and showing reliable potentials in energy management.

2.5. Demonstration of high-efficiency SCSB for portable electronics

Configured with the FPCB-based F-TENG, PMM and the D-MSCs, the high-efficiency self-charging smart bracelet is achieved by assembling all the units among the Ecoflex substrate. The digital photographs of our fabricated smart bracelet are shown in Fig. S11 with complete assembly and corresponding description (Supporting information). When attached among the hand wrist, this bracelet could harvest the mechanical energy from arbitrary human movements, which could be converted into electrical energy through the F-TENG. Through the PMM, the energy could be efficiently stored in D-MSC component and further drive the portable electronics. The proposed scheme of the SCSB is presented in Fig. 5a, which consists of an F-TENG as the AC power source, PMM as the AC-to-DC converter, and D-MSCs as the energy storage device. The external load could be connected to the D-MSCs with the switch divided into energy storage and supply mode.

To verify the self-charging performance, a single MSC is connected to the PMM at the beginning, the ideal charging capability of which is shown in Fig. 5b. Under a continuous process, the charging curve indicates that the smart bracelet owns ideal charging performance with low charge leakage. During the normal walking motion, the stored charges gradually increase with the charging time and the potential
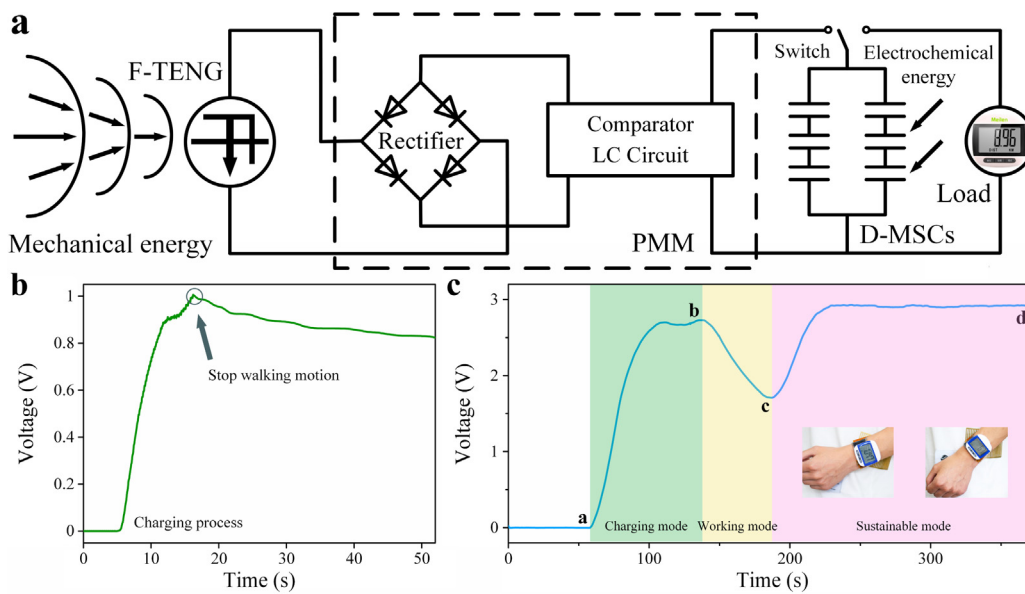
Fig. 5. Application of self-charging smart bracelet for portable electronics. a) Circuit diagram of the SCSB consisting of F-TENG, PMM and D-MSCs with energy harvesting, storing and supply process. b) *V-t* curve of a single MSC charged by the F-TENG and PMM during the walking motion and the self-discharging process. c) *V-t* curve of the SCSB connected to a pedometer under various operating modes, charging mode, working mode, and sustainable mode.

could saturate at nearly 1 V within 8 s. Once we stop the walking motion, the MSC experiences the slowly self-discharging process.

To prove the practical demonstration of our SCSB, it is utilized for simultaneously converting and storing human motion energy and then driving a temperature-humidity meter or pedometer directly. The whole *V-t* curve could be divided into various modes, including the charging mode, working mode and sustainable mode, which is shown in Fig. 5c. At the beginning of charging mode, the linear-like *V-t* curve of SCSB performs steady charging performance with low leakage under a long-time charging procedure (a–b). While the voltage of the SCSB reaches ~3 V, it is utilized to power the pedometer continuously as the working mode (b–c). With the large current of the pedometer due to its initialization routine, the linear drop of *V-t* curve indicates that SCSB is able to drive the pedometer. If we operate the F-TENG again, the pedometer could work sustainably at a steady voltage or even be charged under the fast-operating procedure (c–d). Therefore, the proposed self-charging smart bracelet shows ideal capability as a sustainable micro energy supply for portable electronics.

3. Conclusion

In summary, we have proposed the prototype of self-charging smart bracelet integrated with freestanding triboelectric nanogenerator, power management module and double-sided micro-supercapacitors among the Ecoflex substrate. The smart bracelet could harvest and simultaneously store human motion energy, which could act as wearable power source for self-powered portable electronics. Employed with FPCB technique, the energy harvesting and power management module possess high elasticity and flexibility. Under the hand shaking, the F-TENG could scavenge mechanical energy effectively, which obtain maximum peak power of 300.4 μW and 69.3% energy transfer efficiency. Additionally, the D-MSCs is achieved by laser-patterning and elastomer-transferring method with the CNT-PDMS conductive elastomers. Besides great capacitance, conformability and reliable scalability, the D-MSCs also exhibits long-term and mechanical stability with wide-range working potential. By assembling the F-TENG, PMM and D-MSCs, a self-charging smart bracelet could be achieved for harvesting motion energy and continually powering pedometer as the smart micro energy system. Therefore, this smart bracelet represents a facile approach and promising improvement to develop stretchable and wearable electronics in the practical applications and next generation self-powered systems.

4. Experimental section

4.1. Fabrication of the CNT-PDMS mixture

Firstly, CNT-PDMS elastomer is produced by the solution-evaporation method, where PDMS base resin (Sylgard 184, Dow Corning Co., USA) and multi-walled CNTs (diameter: 10–20 nm, length: 10–30 μm, purity > 98%, Boyu Co., China) are dissolved in toluene (polymer/solvent concentration: 20%). The prepared mixture is magnetic stirred for 4 h until the CNTs are mixed with PDMS thoroughly with the help of the toluene. Subsequently, the sugar templates and cross-linker of PDMS are added to the CNT-PDMS liquid at the weight ratio of 4:1 and 1:10, respectively. Then the mixture is poured into a culture dish to evaporate residual toluene under the magnetic stirring. Finally, the CNT-PDMS-sugar mixture could be obtained after cured at 100 °C for 2 h.

4.2. Fabrication of the D-MSC for energy storage

For the fabrication of D-MSC as energy storage device, we combine laser patterning with elastomer transferring process based on the CNT-PDMS-sugar mixture. Firstly, PMMA mold is patterned with designed interdigital structure through laser-cutting process. Then the prepared CNT-PDMS-sugar mixture is filled into the grooves. To obtain the stretchable energy storage devices, the deformable elastomer substrate Ecoflex (Ecoflex 0030) is developed by mixing a pre-polymer and a curing agent (1:1). Ecoflex elastomer is poured among the PMMA surface and the device is totally dried at 55 °C for 1 h. Peeled off from the PMMA substrate, the CNT-PDMS mixture could be easily transferred to the elastomer film. Then to increase the contact area and ion exchange, the sugar templates are totally dissolved and washed away by soaking in an ultrasonic cleaner at 40 °C. Subsequently, for the gel electrolyte, 6 g phosphoric acid (H_3PO_4) is mixed with 60 ml deionized water and 6 g polyvinyl alcohol (PVA) powder. The mixture is heated up to 85 °C under vigorous stirring until the solution becomes clear. Gel electrolyte is spray coated among the interdigital electrode to form the in-planar MSC. Finally, several MSCs are integrated on the both sides of Ecoflex substrate with alignment and the D-MSCs is successfully prepared.

4.3. Fabrication of energy generating device and power management module

For the energy harvesting device and power management module,

we utilize FPCB technique to fabricate the F-TENG and PMM simultaneously to meet the demands of wearable and flexible applications. Firstly, one sheet of commercial flexible copper clad laminate (FCCL) is prepared, consisting of a flexible polyimide substrate and one copper film with sandwiched thin layer of epoxy adhesive. Employed by the photolithography and etching process, the copper film is patterned to fabricate the comb electrodes and corresponding circuit. For the F-TENG, worked as the electrification material, a layer of polytetrafluoroethylene (PTFE) is laminated on the electrode of slider with a thickness of 50 μm to enhance the output performance during the sliding process. The Ecoflex elastomer is poured onto the bottom surface of FPCB with great flexibility and compatibility.

4.4. Characterization and measurement

Morphologies of the sugar, porous structure and micro-supercapacitor are observed using ESEM (Quanta 600F, FEI Co.) with an operation voltage of 10 kV. A digital oscilloscope (Agilent DSO-X 2014A) is applied to analyze the open-circuit voltage of the F-TENG and self-charging behavior of the SCSB. The short-circuit current is amplified by a SR570 low-noise current amplifier (Stanford Research Systems). Additionally, the performance of the MSC is evaluated by CV and GCD techniques through CS354 electrochemical workstation (CorrTest Co.) with a two-electrode configuration. COMSOL MULTIPHYSICS software is employed to verify the potential distribution simulation.

Acknowledgement

Appendix A. Supplementary material

Supplementary data associated with this article can be found in the online version at doi:10.1016/j.nanoen.2018.10.045.

References

[1] W. Gao, S. Emaminejad, H. Nyein, S. Challa, K. Chen, A. Peck, H. Fahad, H. Ota, H. Shiraki, D. Kiriya, D. Lien, G. Brooks, R. Davis, A. Javey, Nature 529 (2016) 509.
[2] A. Chortos, Z. Bao, Mater. Today 17 (2014) 321.
[3] D. Kim, N. Lu, R. Ma, Y. Kim, R. Kim, S. Wang, J. Wu, S. Won, H. Tao, A. Islam, K. Yu, T. Kim, R. Chowdhury, M. Ying, L. Xu, M. Li, H. Chung, H. Keum, M. McCormick, P. Liu, Y. Zhang, F. Omenetto, Y. Huang, T. Coleman, J. Rogers, Science 333 (2011) 838.
[4] Y. Song, H. Chen, Z. Su, X. Chen, L. Miao, J. Zhang, X. Cheng, H. Zhang, Small 13 (2017) 1702091.
[5] Z.L. Wang, J. Chen, L. Lin, Energy Environ. Sci. 8 (2015) 2250.
[6] Z. Wen, M. Yeh, H. Guo, J. Wang, Y. Zi, W. Xu, J. Deng, L. Zhu, X. Wang, C. Hu, L. Zhu, X. Sun, Z.L. Wang, Sci. Adv. 2 (2016) e1600097.
[7] Y. Song, J. Zhang, H. Guo, X. Chen, Z. Su, H. Chen, X. Cheng, H. Zhang, Appl. Phys. Lett. 111 (2017) 073901.
[8] H. Chen, Y. Song, H. Guo, L. Miao, X. Chen, Z. Su, H. Zhang, Nano Energy 51 (2018) 496.
[9] B. O'Regan, M. Gratzel, Nature 353 (1991) 737.
[10] J. Chen, H. Guo, X. Pu, X. Wang, Y. Xi, C. Hu, Nano Energy 50 (2018) 536.
[11] J. Tarascon, M. Armand, Nature 414 (2001) 359.
[12] P. Simon, Y. Gogotsi, Nat. Mater. 7 (2008) 845.
[13] Y. Song, X. Cheng, H. Chen, J. Huang, X. Chen, M. Han, Z. Su, B. Meng, Z. Song, H. Zhang, J. Mater. Chem. A 4 (2016) 14298.
[14] H. Guo, M. Yeh, Y. Lai, Y. Zi, C. Wu, Z. Wen, C. Hu, Z.L. Wang, ACS Nano 10 (2016) 10580.
[15] Q. Jiang, C. Wu, Z. Wang, A. Wang, J. He, Z.L. Wang, H. Alshareef, Nano Energy 45 (2018) 266.
[16] X. Pu, L. Li, M. Liu, C. Jiang, C. Du, Z. Zhao, W. Hu, Z.L. Wang, Adv. Mater. 28 (2016) 98.
[17] N. Sun, Z. Wen, F. Zhao, Y. Yang, H. Shao, C. Zhou, Q. Shen, K. Feng, M. Peng, Y. Li, X. Sun, Nano Energy 38 (2017) 210.
[18] C. Zhou, Y. Yang, N. Sun, Z. Wen, P. Cheng, X. Xie, H. Shao, Q. Shen, X. Chen, Y. Liu, Z.L. Wang, X. Sun, Nano Res. 11 (2018) 4313.
[19] H. Song, I. Karakurt, M. Wei, N. Liu, Y. Chu, J. Zhong, L. Lin, Nano Energy 49 (2018) 7.
[20] X. Chen, H. Guo, H. Wu, H. Chen, Y. Song, Z. Su, H. Zhang, Nano Energy 49 (2018) 51.
[21] Y. Yang, N. Sun, Z. Wen, P. Cheng, H. Zheng, H. Shao, Y. Xia, C. Chen, H. Lan, X. Xie, C. Zhou, J. Zhong, X. Sun, S. Lee, ACS Nano 12 (2018) 2027.
[22] X. Zhang, M. Han, B. Kim, J. Bao, J. Brugger, H. Zhang, Nano Energy 47 (2018) 410.
[23] J. Chen, Y. Huang, N. Zhang, H. Zou, R. Liu, C. Tao, X. Fan, Z.L. Wang, Nat. Energy 1 (2016) 16138.
[24] X. Cheng, Y. Song, M. Han, B. Meng, Z. Su, L. Miao, H. Zhang, Sens. Actuators A Phys. 247 (2016) 206.
[25] Q. Guan, Y. Dai, Y. Yang, X. Bi, Z. Wen, Y. Pan, Nano Energy 51 (2018) 333.
[26] S. Wang, Y. Xie, S. Niu, L. Lin, Z.L. Wang, Adv. Mater. 26 (2014) 2818.
[27] Y. Xie, S. Wang, S. Niu, L. Lin, Q. Jing, J. Yang, Z. Wu, Z.L. Wang, Adv. Mater. 26 (2014) 6599.
[28] X. Lu, M. Yu, G. Wang, Y. Tong, Y. Li, Energy Environ. Sci. 7 (2014) 2160.
[29] Y. Song, X. Cheng, H. Chen, M. Han, X. Chen, J. Huang, Z. Su, H. Zhang, Micro Nano Lett. 11 (2016) 586.
[30] X. Pu, M. Liu, L. Li, S. Han, X. Li, C. Jiang, C. Du, J. Luo, W. Hu, Z.L. Wang, Adv. Energy Mater. 6 (2016) 1601254.
[31] Y. Song, X. Chen, J. Zhang, X. Cheng, H. Zhang, J. Microelectromech. Syst. 26 (2017) 1055.
[32] J. Maeng, Y. Kim, C. Meng, P. Irazoqui, ACS Appl. Mater. Interfaces 8 (2016) 13458.
[33] Y. Song, H. Chen, X. Chen, H. Wu, H. Guo, X. Cheng, B. Meng, H. Zhang, Nano Energy 53 (2018) 189.
[34] R. Guo, J. Chen, B. Yang, L. Liu, L. Su, B. Shen, X. Yan, Adv. Funct. Mater. 27 (2017) 1702394.
[35] J. Yun, Y. Lim, H. Lee, G. Lee, H. Park, S. Hong, S. Lee, J. Ha, Adv. Funct. Mater. 27 (2017) 1700135.
[36] D. Kim, G. Lee, D. Kim, J. Yun, S. Lee, J. Ha, Nanoscale 8 (2016) 15611.
[37] X. Cheng, L. Miao, Y. Song, Z. Su, H. Chen, X. Chen, J. Zhang, H. Zhang, Nano Energy 38 (2017) 438.
[38] Y. Zi, S. Niu, J. Wang, Z. Wen, W. Tang, Z.L. Wang, Nat. Commun. 6 (2015) 8376.
[39] S. Boisseau, G. Despesse, S. Monfray, O. Puscasu, T. Skotnicki, Smart Mater. Struct. 22 (2013) 025021.
[40] S. Niu, W. Wang, F. Yi, Y. Zhou, Z.L. Wang, Nat. Commun. 6 (2015) 8975.